International Journal of Thermal Sciences, Vol. 110, pp. 270-284, 2016,
DOI: 10.1016/j.ijthermalsci.2016.07.011 (Accepted Version)

Thermohydrodynamics of Bidirectional Groove Dry Gas Seals with Slip Flow

H. Su [1,2], R. Rahmani [2*], H. Rahnejat [2]

[1] School of Mechanical Engineering, Northwestern Polytechnical University, Xi'an Shaanxi, P. R. China

[2] Wolfson School of Mechanical and Manufacturing Engineering, Loughborough University, Loughborough, UK

[*] Corresponding author, Email: R.Rahmani@lboro.ac.uk

Abstract

Thermo-hydrodynamic behaviour of bidirectional dry gas seals with trapezoidal shaped symmetric grooves is studied. A multi-physics model, coupling compressible laminar flow and heat transfer in both the fluid and the solid bodies is used in a multi-physics modelling environment. The multi-physics model also includes slip flow conditions, corresponding to relatively high Knudsen numbers, as well as the effect of asperity interactions on the opposing seal faces. A comparison of the seal performance under isothermal and thermal flow conditions shows the importance of including the thermal effects. The difference in the predicted opening force between isothermal and thermal model can exceed 2.5%, which is equivalent to a force of around 1kN. The importance of designing gas seals to operate at the minimum possible gap to reduce power losses as well as leakage from the contact is highlighted. However, it is shown that there exists a critical minimum gap, below which the power loss in the contact can abruptly increase due to asperity interactions, generating significantly increased operating temperatures.

Keywords: Bidirectional groove dry gas seal; Thermal analysis; Heat transfer; Slip flow; Roughness; Seal performance

Nomenclature

A_s	Side area of the gap
c_p	Specific heat capacity of gas at constant pressure
c_s	Specific heat capacity of seal ring material
D	Outer diameter of the seal ring ($= 2r_o$)
d	Circumferential width of the middle part of groove at outer rim of seal
E	Young's modulus elasticity
E'	Composite Young's modulus of elasticity
F_o	Total opening force (load carrying capacity)
$F_{o,h}$, $F_{o,a}$	Opening force due to hydrodynamic reaction and asperity interactions
$F_{5/2}$, F_2	Statistical functions related to the Greenwood and Tripp asperity model

f	Total friction
f_v,f_b	Viscous and boundary friction
h	Film thickness
h_0	Minimum film thickness
h_c	Critical film thickness
$h_{g,1}$, $h_{g,2}$	Relative depths at the triangular and middle trunk parts of the grooves
h_t	Convection heat transfer coefficient
$h_{t,r}$, $h_{t,s}$	Convection heat transfer coefficient from outer rims of rotor and stator
k	Thermal conductivity of the gas
k_s	Thermal conductivity of seal ring material
Kn	Knudsen number ($= \eta\sqrt{(\pi RT_g/2)}/ph$)
Ma	Mach number ($= r_m\omega/\sqrt{\gamma RT_g}$)
$\dot{m}$	Mass flow rate
N	Rotational speed in RPM
$\hat{n}$	Unit vector in normal direction
n_g	Number of grooves
Nu	Nusselt number ($= h_t D/k$)
P_l	Power loss
p	Pressure
p_{in}, p_{out}	Pressure at the inlet (outer radius) and outlet (inner radius)
Pr	Prandtl number ($= c_p\eta/k$)
$\dot{Q}_l$	Volumetric flow rate of leakage
q	Heat flux
$q_{g,r}$, $q_{g,s}$	Heat flux from gas to rotor and stator contacting faces
$q_{w,r}$, $q_{w,s}$	Heat flux from at the contacting faces of rotor and stator
$q_{z,r}$, $q_{z,s}$	Heat flux in the axial direction at the back faces of rotor and stator
q_r,q_θ,q_z	Heat flux in radial, circumferential and axial directions
R	Specific gas constant
Re	Reynolds number ($= \rho r_m\omega h/\eta$)
Re_D	Reynolds number for convective heat transfer calculations ($= \rho r_o\omega D/\eta$)
r	Radius
r_i, r_o	Inner and outer radius of the seal
r_{g1},r_{g2}	Radius of the bottom rim of lower and upper part of seal groove
r_m	Average radius
r,θ,z	Radial ,circumferential and axial (cylindrical) coordinates
$\hat{r}$,$\hat{\theta}$,$\hat{z}$	Unit vectors in radial, circumferential and axial directions
T_g, T_s	Gas and solid body temperature distribution
$T_{g,0}$, $T_{s,0}$	Inlet gas temperature and initial surface temperature of the seal rings
$T_{g,i}$	Gas temperature at the inlet (outer radius)
$T_{g,r}$, $T_{g,s}$	Gas temperature near rotor and stator contact face surfaces
T_w	Temperature of the solid wall in contact with sealing gas

$T_{w,r}$, $T_{w,s}$	Wall temperature at rotor and stator contact surfaces
t_r, t_s	Axial thickness of the rotating and stationary seals
$\vec{u}_s$	Slip velocity vector
$\vec{V}$	Velocity vector in cylindrical coordinates ($\vec{V} = V_r\hat{r} + V_\theta\hat{\theta} + V_z\hat{z}$)
V_g	Gas velocity magnitude

Greek symbols

α_1, α_2	Spiral groove angle at upper and bottom parts of seal groove
α_v	Tangential momentum accommodation coefficient
γ	Heat capacity ratio
Δ_g	Angle of an annular sector comprising one complete groove
ϵ	Numerical damping coefficients
ε_s	Coefficient of thermal expansion for seal ring
ζ_T	Temperature jump coefficient
η	Dynamic viscosity of gas
κ	Average asperity tip radius
λ	Molecular mean free path
λ_s	Stribeck film ratio parameter
ν	Poisson's ratio
ξ	Asperity density per unit area of the contact
ρ	Gas density
ρ_s	Density of seal ring material
σ	Standard deviation of the surface roughness
σ_s,σ_T	Viscous slip and thermal slip coefficients
ς	Coefficient of boundary shear strength at the tip of asperities
$\bar{\tau}$	Shear stress tensor
$\vec{\tau}_v$	Viscous shear
Φ	Heat source term
φ	Angle of an annular sector of the seal containing a single groove
ω	Angular velocity of rotation

Superscripts

^{n}	Iteration step
^{T}	Transpose of tensor

Subscripts

$_{1,2}$	Rotor, stator
$_c$	Combined
$_{L,R}$	Left and Right hand sides

Abbreviations

AFM	Atomic Force Microscopy
CFD	Computational Fluid Dynamics
DLC	Diamond-Like Carbon

DNS	Direct Numerical Simulation
FEM	Finite Element Method
GUI	Graphical User Interface
LFM	Lateral Force Microscopy
RMS	Root Mean Square
RPM	Revolutions per Minute
SiC	Silicon Carbide

1. Introduction

Non-contacting dry gas seals are widely used in multi-stage compressors such as those employed in the oil and gas industry. Grooves of various shapes have been used on the seal face to induce the required hydrodynamic lift and enhance contact stiffness. This is an additional load carrying contribution to the inherent hydrostatic pressures which also maintain a desired gap between the sealing surfaces. Maintaining a gap is critical in minimising wear and ensuring the reliable operation of the gas seal.

The unidirectional spiral groove gas seals have been the focus of research for many years, unlike the bidirectional seals. The advantages of bidirectional seals is their ability in creating a hydrodynamic lift irrespective of the direction of rotation of the shaft. This feature brings about many operational and maintenance cost benefits (Kowalski and Basu [1]). For instance, some compressors without upgraded control system cannot prevent reverse rotation during shutdown. These would benefit from the lift ability of bidirectional seals. Otherwise, Implementation of preventative reverse rotation control systems can add to the maintenance costs of many existing installations. In addition, the failure of one or more of the adapted compressor control system components can also cause some reverse rotation of the compressor rotor. In such cases and in the absence of hydrodynamic pressure built-up, the hydrostatic pressure alone is not usually sufficient to support the applied closing force, thus causing the seal faces to collapse.

There is a dearth reported research on the performance of bidirectional gas seals. Basu [2] investigated the performance of various groove geometries for bidirectional seals, including the radial or parallel groove profiles. Takeuchi et al [3] introduced bidirectional tapered-step grooves, and a three-row spiral groove configuration was presented by Wang [4]. Goldswain and Do Boer Hignett [5] patented a trapezoidal shape groove configuration for bidirectional seal applications.

Most of studies of isothermal continuum fluid flow conditions in the analysis of bidirectional gas seals (Bonneau et al [6], Zirkelback [7], Xu et al [8], Shahin et al [9], Wang et al [10] and Su et al [11]). Ruan et al [12] showed that in striving to reduce leakage, a tighter seal gap should be used. However, the required minimum gap often can be of the order of seal face roughness, where the probability of direct asperity contact on the opposing surfaces becomes inevitable. Consequently, this would lead to increased frictional losses, generated heat, wear and durability of the seals. Hitherto, such effects have not been addressed in the study of the gas seals to any great detail. Furthermore, with very thin fluid films, the molecular mean free path is comparable with the fluid film thickness itself, thus the assumption of continuum flow

with no slip boundary conditions fails to describe the real physical conditions. Therefore, a modified set of governing equations or associate boundary conditions are required to represent the prevailing conditions (Ruan [13]).

Brunetiere and Modolo [14] showed that with ultra-thin film gaps, sealing performance can be affected by the thermal effects originated from the direct asperity contacts in mixed regime of lubrication. In such applications, where the working fluid is liquid, normally reduced viscosity under high operating temperatures reduce the load carrying capacity of the contact and promote seal seizure. On the other hand, in the case of gas seals and under similar working conditions, the internal heating originated from both viscous and boundary shear can increase the viscosity of gas; resulting in an increase in film thickness, promoting leakage.

Most research; including the aforementioned, have focused on the understanding of the behaviour of unidirectional grooved dry gas seals. For instance, Ruan [13] and Wang and Zhang [15] investigated the effect of slip flow in the spiral groove dry gas seals. Thomas et al [16] and Wang et al [17] included the effect of generated heat on the seal performance, but excluding the effect of any asperity interactions. However, Ruan et al [12] presented a simplified 1D mixed regime of lubrication model for axisymmetric seal contacts with no included grooves. They also investigated the effect of temperature on contact deformation by assuming linear temperature and deformation profiles. Furthermore, they did not include the slip flow conditions in their model, where the gap between the seal faces was of the same order as their roughness. Therefore, there is a need to for a more comprehensive analysis, which should take into account a 2D contact model, incorporating slip flow boundary conditions, asperity interactions in thinner gaps and with the inclusion of thermal effects. Appropriate boundary conditions, taking into account the thermal behaviour of the fluid and solid through a multi-physics approach should also be employed.

This paper extends the previous work of Su et al [11] for the case of bidirectional dry gas seals through inclusion of thermal analysis on the seal performance. Performance of bidirectional gas seals with symmetric trapezoidal grooves under thermal conditions is studied. The multi-physics thermally-coupled model, including fluid flow, heat transfer in both fluid and solids is thus established. Additionally, the effect of slip flow and mixed regime of lubrication are considered. Such an approach has not hitherto been reported in literature. Real measured data from gas seals of compressors in gas conveying pipelines is used in the analysis. The results of isothermal and thermal analyses are compared in order to evaluate the effect of thermal deformation on the seal performance metrics.

2. Numerical Model

2.1. Flow conditions

For a typical gas seal configuration, the flow of gas through the contact and the associated frictional losses is expected to increase with elevated temperature of the fluid, as well as the surrounding solid boundaries. These increased losses are due to heat convection and conduction processes. With the included surface grooves, the generated frictional power loss

is expected to be non-uniform, which may cause thermal distortion of the solid bodies. Simultaneously, the temperature of the entrant gas flow into the contact rises because of the relatively hotter surfaces, which in turn can increase the viscosity of the gas, thus the viscous frictional losses. However, increased gas viscosity is expected to increase the load carrying capacity and result in a larger gap between the sealing surfaces. A larger gap would reduce the chance of direct boundary interaction, decreasing the power loss due to boundary friction. There is also the increased chance of gas leakage with increasing gaps. Therefore, there are complex interactions in coupled thermal conditions, gas flow, mechanical distortion and surface interactions, requiring a representative multi-physics analysis.

The choice of a model and the associated boundary conditions is based on the physical operating conditions; temperature, contact pressure, rotational speed, and the designed seal face gap. Reynolds', Knudsen and Mach numbers determine the type of gas flow, in terms of flow compressibility, laminarity and the need for any slip flow boundary conditions.

Reynolds' number indicates the permissible range for an assumed laminar flow. It can be shown that the Reynolds' number remains below 4000 in the current analysis. This indicates that the conditions studied here fall largely in the realm of the laminar gas flow, particularly for low speed operations with fairly small gaps. This is the range of interest in the current study and an increasing trend in practice, where there is a greater probability of direct asperity contacts. However, a more accurate analysis may need to consider the turbulent flow conditions and use an appropriate turbulent model. These conditions would lead to higher film thickness, lower load carrying capacity and potential leakage.

The gas density, in general, is a function of temperature and pressure. For lower Mach numbers, incompressible flow conditions may be assumed. The typical Mach numbers encountered fall below 0.25, yielding an incompressible gas flow. However, for the sake of generality, the fluid flow is considered to be compressible throughout this study, whilst the effect of the compressive heating is neglected.

For gas flow the Knudsen number is commonly used to ascertain any degree of gas rarefaction. For: $\mathrm{Kn} < 0.01$, a continuum flow with no slip boundary conditions may be assumed, whilst for $0.01 \leq \mathrm{Kn} < 15$, requires slip flow boundary conditions (Szeri [18]). For some of the studied cases in this paper, the Knudsen number can take values greater than 0.01 and hence, slip boundary conditions are defined. It should also be noted that the inspection of the Knudsen number in this study does not predict any molecular flow regime conditions.

2.2. Contact geometry

The studied seal pair constitutes a nominally flat working surface for the stationary ring (stator) and a rotating ring (rotor), containing symmetric trapezoidal shaped grooves. Due to the symmetrical distribution of the grooves around the seal face, one can simulate an annular slab comprising a single groove feature. This is a common computational approach (Ruan [13], Shahin et al [9], Wang et al [17] as well as other similar works).

Figure 1 depicts the schematic profile of a single groove computational domain.

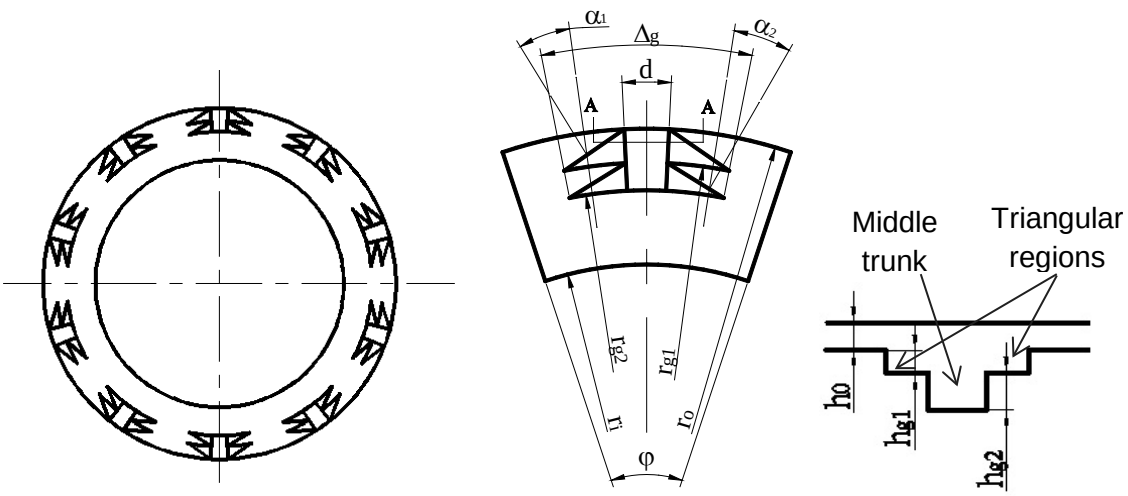

(a) (b) (c)

Figure 1: (a) Whole geometry of the rotor face, (b) An annular sector of the seal face with the trapezoidal shaped geometry, and (c) Side view (cross-section A-A) of the annular slab

Therefore, local gap or film thickness at any point in the contact can be defined as:

$$h(r,\theta) = \begin{cases} h_0 & \text{over non} - \text{grooved area (land)} \\ h_0 + h_{g,1}(r,\varphi) & \text{over triangular part of groove} \\ h_0 + h_{g,1}(r,\varphi) + h_{g,2}(r,\varphi) & \text{over central part of groove} \end{cases} \quad (1)$$

where, h_0 is the minimum film thickness, representing the gap between the flat (non-grooved) parts of the rotor and the stator surface. For transient operating conditions, the minimum gap is a function of time due to the variations in load and/or rotational speed. However, for steady state (quasi-static) conditions, the minimum gap is obtained through a force balance between the applied load and the reacting hydrodynamic and asperity contact forces. This is further later.

2.3. Governing equations for gas flow

For a compressible and iso-viscous steady state flow, the governing continuity and Navier-Stokes momentum equations in the absence of any body force such as gravity in the following vector form are (Munson et al [19]):

$$\vec{\nabla} \cdot \left(\rho \vec{V}\right) = 0 \quad (2)$$

$$\rho\left(\vec{V} \cdot \vec{\nabla}\right)\vec{V} = -\vec{\nabla}p + \eta\vec{\nabla}^2\vec{V} \quad (3)$$

where, in cylindrical coordinates the gradient, convective and vector Laplacian operators take the forms:

$$\vec{\nabla} \equiv \left(\frac{\partial}{\partial r} + \frac{1}{r}\right)\hat{r} + \frac{1}{r}\frac{\partial}{\partial \theta}\hat{\theta} + \frac{\partial}{\partial z}\hat{z} \quad (4)$$

$$\vec{V} \cdot \vec{\nabla} \equiv V_r \frac{\partial}{\partial r} + V_\theta \frac{1}{r}\frac{\partial}{\partial \theta} + V_z \frac{\partial}{\partial z} \quad (5)$$

$$\vec{\nabla}^2 \vec{V} \equiv \left(\nabla^2 V_r - \frac{1}{r^2}V_r - \frac{2}{r^2}\frac{\partial V_\theta}{\partial \theta}\right)\hat{r} + \left(\nabla^2 V_\theta - \frac{1}{r^2}V_\theta + \frac{2}{r^2}\frac{\partial V_r}{\partial \theta}\right)\hat{\theta} + \nabla^2 V_z \hat{z} \quad (6)$$

In the last equation, the ordinary Laplacian operator in cylindrical coordinates is defined as:

$$\nabla^2 \equiv \frac{1}{r}\frac{\partial}{\partial r}\left(r\frac{\partial}{\partial r}\right) + \frac{1}{r^2}\frac{\partial^2}{\partial \theta^2} + \frac{\partial^2}{\partial z^2} \quad (7)$$

In addition, the energy equation for the fluid flow with variable thermal conductivity and specific heat capacity under steady state conditions, neglecting the effect of heat-induced compressibility becomes:

$$\rho\left(\vec{V} \cdot \vec{\nabla}\right)\left(c_p T_g\right) - \vec{\nabla} \cdot \left(k\vec{\nabla} T_g\right) = \Phi \quad (8)$$

where, Φ is the heat source term, which mainly originates from the frictional losses in the contact.

2.4. Constitutive equations for gas properties

The sealing gas is considered to have the properties of air, thus following the ideal gas behaviour; i.e. $\rho = p/RT_g$. The thermal and mechanical properties of the gas are considered to be variable with temperature only. Hence, the following empirical relationships obtained through data fitting are used to describe the variations of gas dynamic viscosity, η, thermal conductivity, k, and specific heat capacity at constant pressure, c_p, with temperature [20]:

$$\eta(T) = -8.38278 \times 10^{-7} + 8.35717 \times 10^{-8} T_g - 7.69430 \times 10^{-11} T_g^2 + 4.64373 \times 10^{-14} T_g^3 - 1.06586 \times 10^{-17} T_g^4 \quad (9)$$

$$k(T) = -2.27584 \times 10^{-3} + 1.15480 \times 10^{-4} T_g - 7.90253 \times 10^{-8} T_g^2 + 4.11702 \times 10^{-11} T_g^3 - 7.43864 \times 10^{-15} T_g^4 \quad (10)$$

$$c_p(T) = +1.04764 \times 10^{3} - 3.72589 \times 10^{-1} T_g + 9.45304 \times 10^{-4} T_g^2 - 6.02409 \times 10^{-7} T_g^3 + 1.28590 \times 10^{-10} T_g^4 \quad (11)$$

At each computational iterative step the gas properties are updated, based on the calculated gag temperature at the instantaneous iteration step until a steady state solution is achieved.

2.5. Slip flow conditions

For the cases where: Kn ≥ 0.01, the slip flow conditions are considered. In the slip flow regime, the Navier-Stokes equations can be used to model the flow of the gas, except within a thin layer of rarefied gas adherent to the solid boundaries; known as the Knudsen layer

(Fukui and Kaneko [21]). The effect of Knudsen layer on the continuum part of the flow can be modelled by modifying the boundary conditions for the Navier-Stokes equations. Using the generalised form of the Maxwell's definition, the slip boundary conditions for the velocity and temperature at the solid walls are described as [22]:

$$\vec{u}_s = \sigma_s \frac{\lambda}{\eta}[\bar{\tau}\hat{n} - (\hat{n}^T\bar{\tau}\hat{n})\hat{n}] + \sigma_T \frac{\eta}{\rho T}\left[\vec{\nabla}T_w - \left(\hat{n}\cdot\vec{\nabla}T_w\right)\hat{n}\right] \quad (12)$$

$$T_w = T_g - \zeta_T \lambda \left(\hat{n}\cdot\vec{\nabla}T_g\big|_w\right) \quad (13)$$

where, the second term on the right-hand-side of equation (12) accounts for thermal creep, generating slip velocity in the fluid flow opposing the direction of the tangential heat flux (Gad-el-Hak [23]). Furthermore, in the equations above, $\vec{u}_s$ is the slip velocity vector, $\hat{n}$ is the contact normal to the boundary solids, $\bar{\tau}$ is the viscous shear stress tensor, λ is the molecular mean free path, η is the gas dynamic viscosity and ρ, its the density. T is the gas temperature and T_w is the solid wall temperature in contact with the sealing gas flow. In addition, the parameters; σ_s , σ_T and ζ_T represent viscous slip, thermal slip and temperature jump coefficients within the generalised Maxwellian model, and are defined as [22]:

$$\sigma_s = \frac{2-\alpha_v}{\alpha_v}, \qquad \sigma_T = \frac{3}{4}, \qquad \text{and} \qquad \zeta_T = \sigma_s \frac{2\gamma}{\gamma+1}\frac{k}{\eta c_p} \quad (14)$$

where, α_v is the dimensionless coefficient of tangential momentum accommodation. This is typically dependent on the fluid and solid body types and the surface finish, and is determined experimentally. It can generally vary between 0.2 to 1.0 (Gad-el-Hak [23] and Karniadakis et al [24]). The lower limit is for exceptionally smooth surfaces and the upper limit is used for most practical engineering surfaces (Gad-el-Hak [23]). Considering the roughness of the surfaces used in this study, a value of 0.9 is employed for the coefficient of tangential momentum accommodation.

2.6. Boundary conditions for the fluid flow

The boundary conditions for pressure at the inner and outer rim radii and along the circumferential and axial directions of the seal are considered to remain constant as:

$$p(r_i, \theta, z) = p_{out}, \qquad \text{and} \qquad p(r_o, \theta, z) = p_{in} \quad (15)$$

Furthermore, periodic-type boundary conditions are assumed at the two lateral sides of the annular sector (slab) of the seal. As a result the pressure gradient at any radial position over the circumferential boundaries is set zero. In addition, the continuity of flow condition determines that the mass flow into and out of the contact in the circumferential direction should equate, thus [25-26]:

$$\left.\frac{\partial p}{\partial \theta}\right|_{(r,\theta_L)} = \left.\frac{\partial p}{\partial \theta}\right|_{(r,\theta_R)} = 0 \quad (16)$$

$$\dot{m}(r,\theta_L) = \dot{m}(r,\theta_R) \tag{17}$$

2.7. Heat conduction in the solid bodies

The temperature distribution in the solid bodies is governed by heat conduction. To provide a complete thermal model, this requires the solution of heat conduction in the solids (i.e. for the rotating and stationary seal faces with coupled thermal boundary conditions between the fluid and the solid boundaries). In the current analysis the heat transfer due to radiation is neglected and therefore, the focus is put upon conductive heat transfer. In addition, both stator and rotor are considered to be homogenous and isotropic solids.

The heat conduction equation for the rotor without an internal heat source in cylindrical coordinates is (Noda et al [27]):

$$\rho_s c_s \omega \frac{\partial T_s}{\partial \theta} = k_s \nabla^2 T_s \tag{18}$$

For the stator, the heat condition reduces to its steady state form, thus:

$$\nabla^2 T_s = 0 \tag{19}$$

2.8. Thermal boundary conditions and gas/solid temperature coupling

The outer rim of the rotor and the stator rings are exposed to the ambient and the compressor chamber fluids respectively. In both cases, there is a relative motion between the solid body and the surrounding fluid. Therefore, forced convective heat transfer for the outer rims is considered. The convection heat transfer coefficient is defined as (Incropera et al [28]):

$$h_t = \frac{\mathrm{Nu}k}{D} \tag{20}$$

where, k is the thermal conductivity of the surrounding fluid, which is assumed to be air, $D = 2r_o$ is the diameter of the seal ring and Nu is the Nusselt number. The surface-averaged Nusselt number for forced convective heat transfer for a cylinder in crossflow is given by the Churchill-Bernstein equation (Incropera et al [28]):

$$\mathrm{Nu} = 0.3 + \frac{0.62\mathrm{Re}_D{}^{1/2}\mathrm{Pr}^{1/3}}{\left[1+(0.4/\mathrm{Pr})^{2/3}\right]^{1/4}}\left[1+\left(\frac{\mathrm{Re}_D}{282000}\right)^{5/8}\right]^{4/5} \quad \text{where, } \mathrm{PrRe}_D \geq 0.2 \tag{21}$$

In this equation, Re_D is the Reynolds' number and is defined, based on the cylinder diameter as the characteristic length. In addition, in the case of the rotor disc, the characteristic speed is considered to be $r_o\omega$. For the case of the stator, the characteristic speed is considered to be the gas flush speed in the chamber, which in this case is taken as 5m/s, based on the recommendation by Wang et al [17].

In the inner rim of the seal rings, adiabatic boundary conditions are used. In reality, the inner rims of the seal rings are connected to the supporting shafts which can further aid heat transfer away from the gas seal rings. Therefore, a more realistic boundary condition needs to take into account the entire assembly, which is beyond the scope of the current analysis. Therefore, at the inner rims:

$$-\hat{n}.\,q_r = 0 \tag{22}$$

Periodic heat boundary conditions are assumed for the two lateral faces of the annular sector of both the rotor and the stator in the circumferential direction. These boundary conditions are defined as:

$$-\hat{n}_L q_{\theta_L} = \hat{n}_R q_{\theta_R}, \quad \text{and} \quad T_{s,L} = T_{s,R} \tag{23}$$

where, q_θ denotes the heat flux from the solid surface at either sides of the annular sector in the circumferential direction.

For back surfaces of both the seal rings in the axial direction, adiabatic boundary conditions are assumed, which are defined as:

$$\hat{n}.\,q_{z,r} = -\hat{n}.\,q_{z,s} = 0 \tag{24}$$

The boundary conditions for the surfaces of the seal rings contact faces constitute the heat flux produced due to contact friction. The heat generated due to viscous shear of the fluid and any asperity interaction under given operational conditions is transferred through the fluid to the boundary solids. The heat flow from the gas should be coupled to those in the solid rotor and stator by applying the continuity of heat flux condition and conformance of temperatures at the interface. In other words, the temperature and heat flux in the interface of fluid and solid should be the same, thus:

$$q_{w,r} = q_{g,r}, \quad q_{w,s} = q_{g,s}, \quad \text{and} \quad T_{w,r} = T_{g,r}, \quad T_{w,s} = T_{g,s} \tag{25}$$

Figure 2 below is a schematic representation of the implemented thermal boundary conditions in the current analysis.

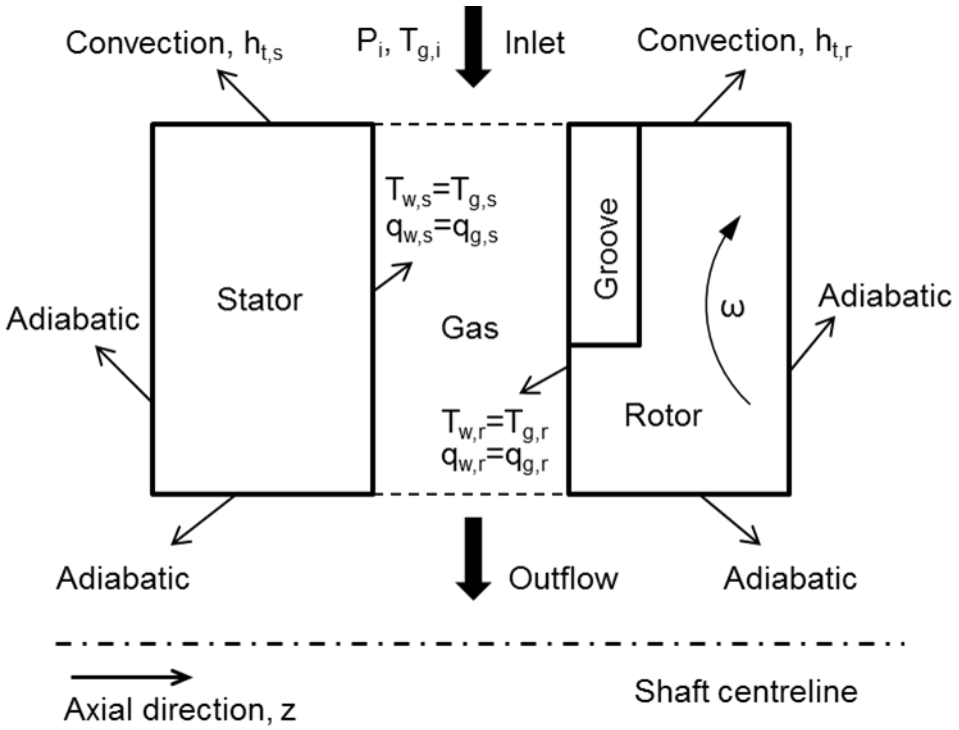

Figure 2: Schematic representation of the thermal boundary conditions

2.9. Total load carrying capacity (opening force)

Contact pressure distribution is obtained through numerical solution of the governing equations in an iterative manner. Once the convergence criteria are satisfied, the contact pressure distribution is evaluated. Further details on the solution methodology are given in Section 3. Integrating the contact pressure distribution gives the gas hydrodynamic load carrying capacity, or the opening force as is usually known in the gas seal analysis terminology parlance:

$$F_{o,h} = n_g \int_{r_i}^{r_o} \int_{\varphi_L}^{\varphi_R} p r d\varphi \, dr \tag{26}$$

In addition, if the film ratio is sufficiently low (i.e. $\lambda_s = \frac{h}{\sigma_c} < \sim 3$), then the interacting asperities would also contribute to the load carrying capacity of the contact. The load carried by the asperities on the opposing rough surfaces is given by Greenwood and Tripp [29] as:

$$F_{o,a} = n_g \frac{16\sqrt{2}}{15} \pi (\xi_c \kappa_c \sigma_c)^2 \sqrt{\frac{\sigma_c}{\kappa_c}} E' \int_{r_i}^{r_o} \int_{\varphi_L}^{\varphi_R} F_{5/2}(\lambda_s) r d\varphi \, dr \tag{27}$$

where, E' is the equivalent Young's modulus of elasticity of the rotor and stator rings (surfaces 1 and 2, respectively), σ_c, the combined standard deviation of the asperity peaks, combined average radius of curvature of asperity peaks, κ_c, the combined standard deviation of the asperity peaks, and ξ_c, the combined surface density of the asperity peaks, which are defined as:

$$\frac{1}{E'}=\frac{1-\nu_1^2}{E_1}+\frac{1-\nu_2^2}{E_2} \qquad \sigma_c=\sqrt{\sigma_1^2+\sigma_2^2}, \qquad \frac{1}{k_c}=\frac{1}{\kappa_1}+\frac{1}{\kappa_2}, \quad \text{and} \quad \xi_c=(\xi_1+\xi_2)/2 \tag{28}$$

In addition, the statistical function $F_{5/2}$ can be approximated using a 5th-order polynomial curve fit as (Gohar and Rahnejat [30]):

$$F_{5/2}(\lambda_s)=\max\{-0.0046\lambda_s^5+0.0574\lambda_s^4-0.2958\lambda_s^3+0.7844\lambda_s^2-1.0776\lambda_s+0.616,0\} \tag{29}$$

The above equation indicates that for negative values of the function $F_{5/2}$, the value of the function should be set to zero. This occurs when the local gap is large enough to ensure that the opening force is entirely due to the hydrodynamic reaction.

Thus, the total opening force (load carrying capacity) for the contact becomes:

$$F_o=F_{o,h}+F_{o,a} \tag{30}$$

2.10. Frictional power loss

Viscous friction is:

$$f_v=n_g\int_{r_i}^{r_o}\int_{\varphi_L}^{\varphi_R}|\vec{\tau}_v|r d\varphi\, dr \quad \text{where, } \vec{\tau}_v=\tau_{v,r}\hat{r}+\tau_{v,\theta}\hat{\theta} \tag{31}$$

Under purely hydrodynamic conditions, the contribution due to viscous shear of the fluid film accounts for the contact friction. However, when mixed regime of lubrication prevails ($\lambda_s<\sim 3$), then contribution due to boundary friction occurs as the result of direct asperity interactions on the opposing rough seal faces. The boundary friction is calculated as:

$$f_b=\varsigma F_{o,a} \tag{32}$$

where, ς is the coefficient of boundary shear strength at the tip of asperities, which takes into account adhesive and any ploughing deformation friction. This is analogous to coefficient of friction at asperity level and is usually obtained using an Atomic Force Microscope (AFM), utilised in Lateral Force Microscopy (LFM) mode. The procedure for measuring ς for real engineering surfaces is shown in Styles et al [31]. The same procedure was followed for the current analysis to obtain the exact ς value for the seal materials which are used in the current analysis.

The AFM measurements resulted in a coefficient of boundary shear strength of $\varsigma=0.382$. It should be noted that this was for a used seal surface, which included any surface oxidation and impregnated contaminants through in-field use. These were not chemically removed in order to obtain representative in-service conditions.

The total friction in the contact can thus be represented as:

$$f = f_v + f_b = n_g \left[\int_{r_i}^{r_o} \int_{\varphi_L}^{\varphi_R} |\vec{\tau}_v| r d\varphi \, dr + \frac{16\sqrt{2}}{15} \pi (\xi_c \kappa_c \sigma_c)^2 \sqrt{\frac{\sigma_c}{\kappa_c}} E' \varsigma \int_{r_i}^{r_o} \int_{\varphi_L}^{\varphi_R} F_{5/2}(\lambda_s) r d\varphi \, dr \right] \quad (33)$$

Finally, the total frictional power loss in the contact is calculated as follows:

$$P_l = n_g \omega \left[\int_{r_i}^{r_o} \int_{\varphi_L}^{\varphi_R} |\vec{\tau}_v| r^2 d\varphi \, dr + \frac{16\sqrt{2}}{15} \pi (\xi_c \kappa_c \sigma_c)^2 \sqrt{\frac{\sigma_c}{\kappa_c}} E' \varsigma \int_{r_i}^{r_o} \int_{\varphi_L}^{\varphi_R} F_{5/2}(\lambda_s) r^2 d\varphi \, dr \right] \quad (34)$$

2.11. Heat generated in the contact (heat source term)

In general, the energy dissipated in the contact causes an incremental rise in the flowing gas temperature, as well as the surrounding solid boundaries. In addition, these losses can produce acoustic emissions from the contact which also contribute to the thermo-elastodynamic deformation. In the current study it is assumed that the entire dissipated contact energy contributes to the heat source term, Φ, in equation (8). Thus, the heat source term, which is in the form of power per unit volume becomes:

$$\Phi = \frac{P_l}{\int_{r_i}^{r_o} \int_0^{2\pi} \int_0^{h(r,\theta)} dz r d\varphi dr} \quad (35)$$

2.12. Leakage from the contact

The volumetric rate of leakage flow is calculated by integrating the flow flux over the outer and the inner rims of the computational domain as:

$$\dot{Q}_l = n_g \oiint \vec{v} d\vec{A}_s \quad (36)$$

where, A_s is the total side area of the gap around the edges of the computational domain (leakage area) and $\vec{v}$ is the velocity vector at the boundaries.

3. Method of Solution

By assuming an initial minimum film thickness (gap), temperature and pressure distributions, the pressure and velocity flow fields are determined through solution of the governing equations and associated boundary conditions, provided in subsections 2.3 to 2.8.

In the current study the commercially available COMSOL multi-physics software (V5.1) was used to solve the Navier-Stokes and energy equations for the conjunctional flow field with the heat transfer to the solid body and slip flow boundary conditions described in the previous sections. The relevant equations and the associated boundary conditions can easily be selected from the available options in the software GUI. The equations are solved using the embedded FEM software. The in-built FEM solver divides the computation domain into the

computational elements of various types, including quadrilateral, tetrahedral or a mixture of both. A typical computational mesh used in the current analysis is shown in Figure 3. A total number of 171,311 elements were used. A mixed mesh tetrahedral and quadrilateral elements were employed for both fluid and solid computational domains.

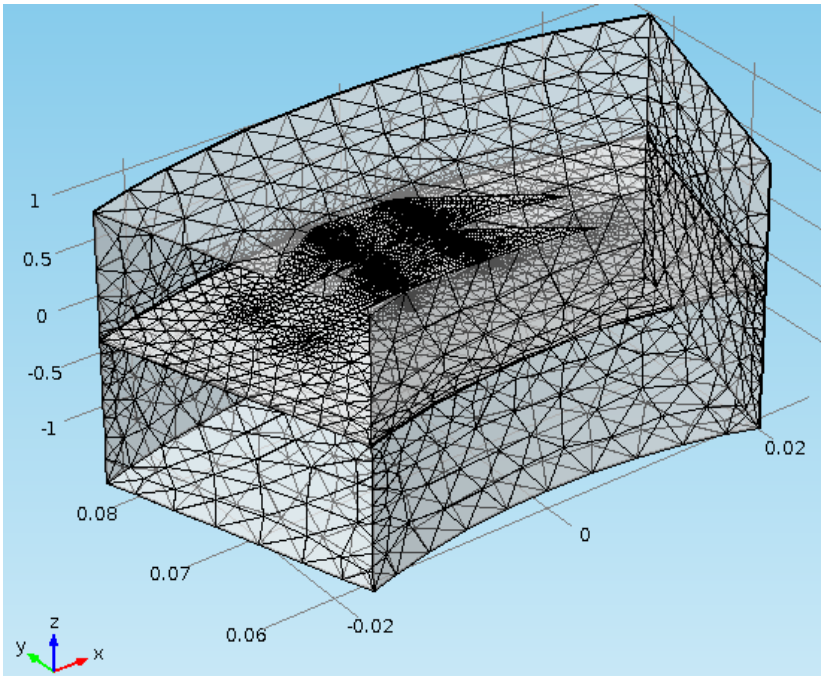

Figure 3: Computational domain with the unstructured mesh elements

The quality of meshes and the mesh-dependency of the results to the type, size and distribution of the meshes were all examined. Table 1 lists the variations in the calculated opening force as the number of computational mesh elements increase. The computational time for each case is also listed in this table.

Table 1: Dependency of the results on mesh density and associated computational time

Number of mesh elements	Opening force (N)	Computational time (s)
58445	39631	248
92508	39803	431
156252	39887	797
171311	39935	920
201244	39939	4813

Quasi-static load balance is sought between the applied load (closing force) and the load carrying capacity of the contact (opening force). This is necessary in order to obtain the minimum contact film thickness (gap). The load balance is:

$$\sum(F)_z = 0 \Rightarrow F_c = F_o \quad (37)$$

Under the given operating conditions, this load balance can be achieved at only a certain minimum gap. Therefore, through an iterative solution method for the load balance equation, it is possible to find the actual minimum gap under the prescribed conditions. At each iteration step, the minimum gap is updated using the following relationship (Rahmani et al [32]):

$$h_0^{n+1} = \left(1 + \epsilon \frac{F_o - F_c}{\max\{F_o, F_c\}}\right) h_0^n \quad (38)$$

where, ϵ is a damping coefficient, determined empirically with a typical value of 0.05. At each iteration step, the governing equations for the fluid flow and heat transfer are solved.

The load convergence iterations were terminated, when the calculated error based on the difference ratio between the opening and closing forces complies with the condition: $|F_o - F_c|/F_c < 10^{-3}$.

Figure 4 provides the flowchart for the computational procedure employed in the current study.

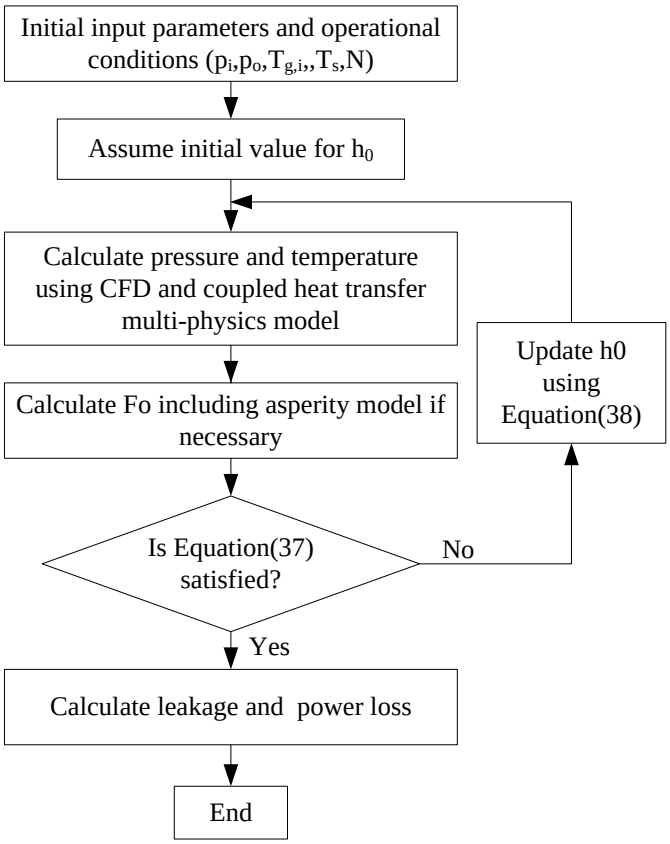

Figure 4: Flowchart of computational procedure

4. System Specifications

4.1. Geometrical data

The geometrical parameters required to define the contact geometry are listed in Table 2.

Table 2: Geometrical parameters of the seal pair

Parameter	Value	Unit
Outer radius, r_o	85.23	mm
Inner radius, r_i	60.01	mm
Number of grooves, n_g	10	-
Rotor axial thickness, t_r	11.08	mm
Stator axial thickness, t_s	12.65	mm
Triangular groove depth , h_{g1}	5.27	µm
Middle groove depth, h_{g2}	18.5	µm
Bottom rim radius of lower groove, r_{g2}	73.38	mm
Bottom rim radius of upper groove, r_{g1}	78.92	mm
Upper groove spiral angel, α_1	27	°
Lower groove spiral angle, α_2	27	°
Grooved area angle, Δ_g	22.21	°
Middle trunk groove width, d	8.4	mm

4.2. Thermo-mechanical properties of the seal materials

Both rotary and stationary seal rings are made of silicon carbide (SiC). Although the stator seal surface contains a diamond-like carbon (DLC) coating, for the purpose of this study and to avoid further complexity in the analysis, it was assumed that the DLC has similar thermo-mechanical properties as the substrate SiC material. In reality, existence of coatings such as DLC can affect the tribological conditions. At low operational gaps, when asperities on opposing surface come into contact, the presence of coatings can provide certain degree of lubricity and hence alter the generated friction. This would also affect heat generation and the thermal deformation of the sealing surfaces, resulting in different forms of structural deformation and induced thermal stresses between the coating and the substrate material. A further in-depth study would be required for further understanding of the consequences in the seal design.

The thermo-mechanical properties are listed in Table 3.

Table 3: Thermo-mechanical properties of the seal pair material

Parameter	Value	Unit
Young's modulus of elasticity, E	420	GPa
Poisson's ratio, ν	0.14	-
Thermal conductivity, k_s	120	W/m.K
Specific heat capacity, c_s	750	J/kg.K
Density, ρ_s	3100	kg/m^3
Coefficient of thermal expansion, ε_s	4×10^{-6}	K^{-1}

4.3. Surface topography

The topographical data are required for the asperity contact model. These are obtained using Alicona Infinite Focus Microscopy with a nominal vertical resolution of ±1nm. The measured seal surface roughness parameters are listed in Table 4. It should be noted that for the current analysis, samples of used seal rings were employed to reflect the real in-field working conditions.

Table 4: Surface topography information for the rotor and stator seal surfaces

Parameter	Value	Unit
RMS surface roughness of rotating face, σ_1	0.031	µm
Asperity density per unit area of the contact for rotating face, ξ_1	2470.25	mm^{-2}
Average asperity tip radius for rotating face, κ_1	57.22	µm
RMS surface roughness for stationary face, σ_2	0.344	µm
Asperity density per unit area of the contact for stationary face, ξ_2	2282.33	mm^{-2}
Average asperity tip radius for stationary face, κ_2	24.60	µm
Combined surface roughness, σ_c	0.345	µm
Combined asperity density per unit area of the contact, ξ_c	2376.29	mm^{-2}
Combined asperity tip radius, κ_c	17.20	µm

Using the data in Table 4, critical film thickness below which the asperity interaction can occur is calculated. By solving equation (29), the critical film ratio is found to be $\lambda_s \cong 2.23$. Given that the combined surface roughness from Table 4 is $\sigma_c = 0.345$, the critical film thickness is obtained as: $h_c \cong 0.77$ µm.

4.4. Operating conditions

The operating conditions of gas seals vary within a wide range, depending on the application and requirements. The operational conditions for the purpose of current analysis are listed in Table 5.

Table 5: Specifications of operating conditions

Parameter	Value	Unit
Pressure at inlet, p_{in}	4.5, 1.0	MPa
Pressure at outlet, p_{out}	0.101	MPa
Inlet gas temperature, $T_{g,in}$	300, 423	K
Initial temperature of seal surfaces, $T_{s,0}$	300	K
Rotation speed, N	2000-11370	RPM

5. Validation of the Numerical Model

The developed model is validated through comparing its predictions with the results of other studies. Figure 5 shows such a comparison with the findings of Wang et al [17], who employed a Direct Numerical Simulation (DNS) method, as well as with the results of Wang et al [33], using ANSYS-CFX software tool. In general, good agreement is observed between the results of the current study with those stated above.

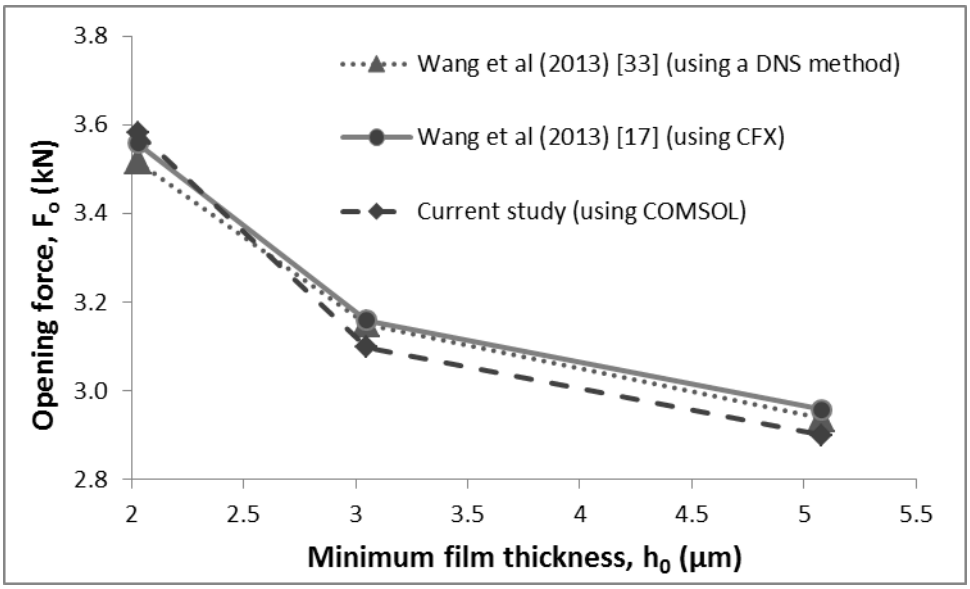

Figure 5: Validation of the numerical model

6. Results and Discussion

The results are presented in three stages. Firstly, the local variations of important performance parameters, including pressure, velocity and temperature distributions are discussed. Secondly, the importance of including the thermal model and its effects on the

performance parameters is highlighted. This comparison is made for predicted results with thermal and isothermal models. Thirdly, the effect of asperity interactions with the incidence of thin films, leading to a mixed regime of lubrication is investigated.

6.1. Local variations in pressure, temperature and velocity field

The local variations in pressure, temperature and velocity flow field are shown in various cross-sections in the axial and radial directions. These cross-sections are shown in Figure 6. In Figure 6a, the axial cross-sections; 1, 2, 3 and 4 refer to those through the centre of the gas film, at the rotor surface, at the centre of the triangular part of the groove, and finally through the centre of the middle trunk of the groove respectively. In Figure 6b, the radial cross-sections correspond to: $r = 70$, 75 and 82mm, respectively. The results shown here are for an inlet pressure of $p_{in} = 4.5$ MPa, and an outlet pressure of $p_{out} = 0.1$ MPa, with the gas inlet temperature of $T_{g,i} = 423$ K, and a minimum film thickness of $h_0 = 3$ μm. The rotational speed is $N = 11{,}370$ RPM in the clockwise direction.

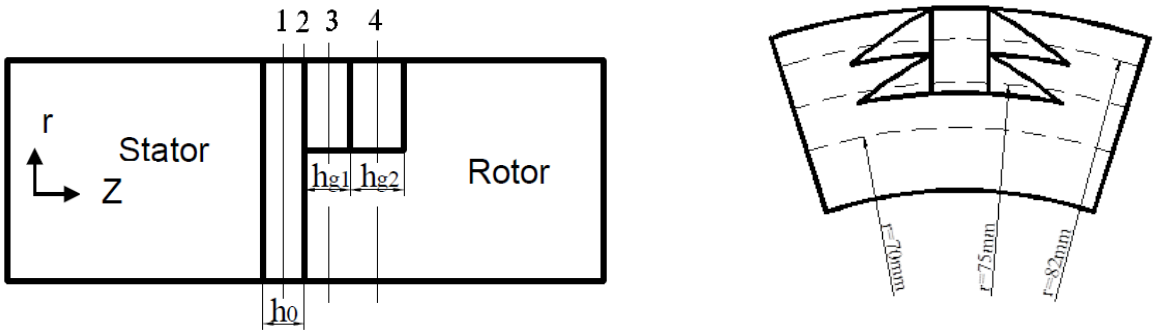

(a) (b)

Figure 6: Position of (a) axial and (b) radial cross-sections

Figure 7 shows the pressure distribution at the 4 aforementioned axial cross-sections (Figure 6a). The direction of rotor rotation is also shown. Figures 7a and b show that the gas pressure at the left-hand-side of the groove is much higher (as it would be expected), given the direction of the motion. In addition, in Figures 7a and b the higher pressures at the inlet (outer rim) of the seal are gradually reduced towards the inner rim radius. However, inside the groove (Figures 7c and d), the pressure distribution is dominated by the gas swirl and the hydrostatic pressure has a negligible effect.

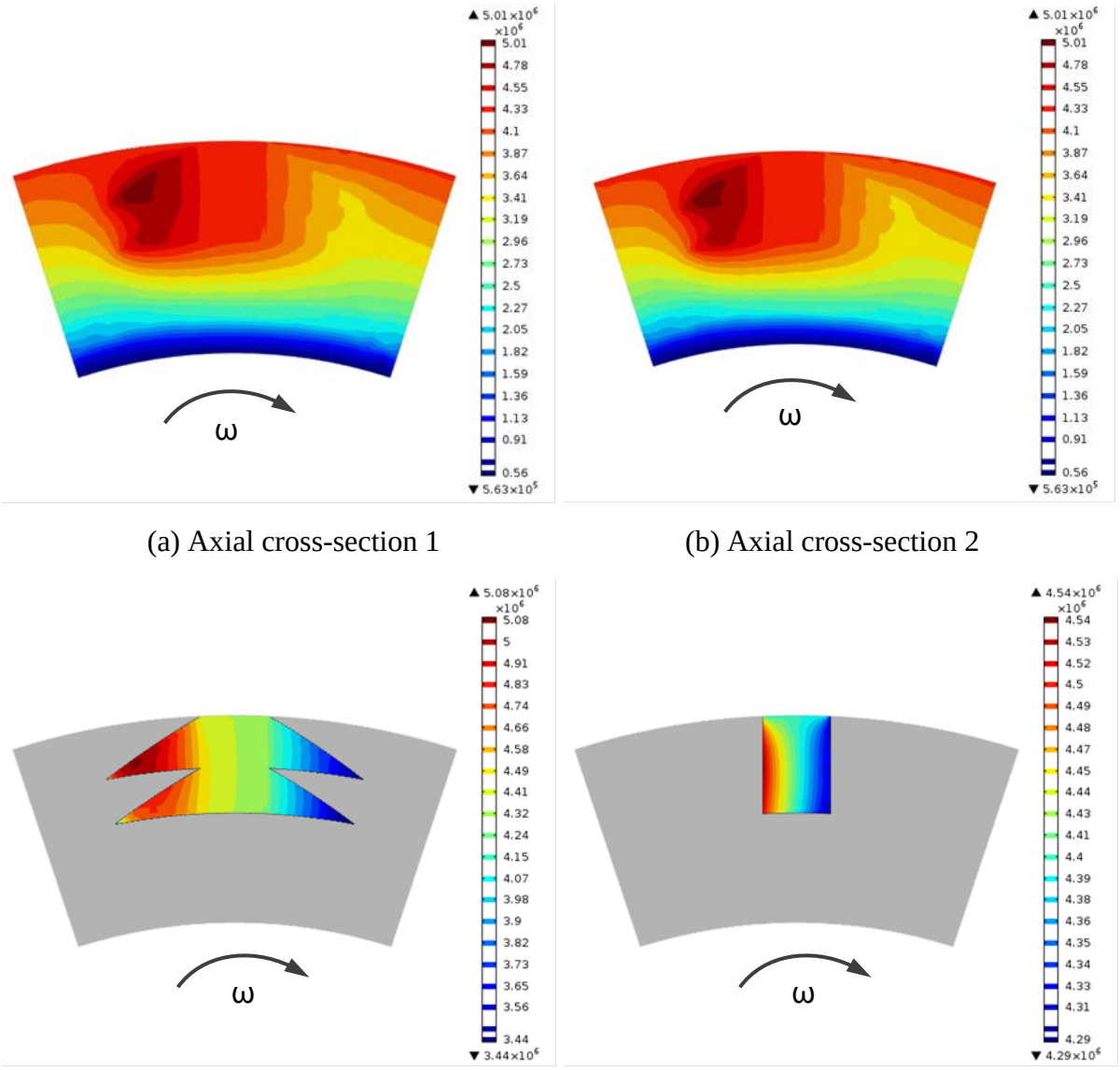

(a) Axial cross-section 1 (b) Axial cross-section 2

(c) Axial cross-section 3 (d) Axial cross-section 4

Figure 7: Pressure distribution (in Pa) at different axial cross-sections

Figure 8 shows the contours of velocity flow field, varying in a similar manner as the pressure variation in Figure 7. Figure 8a shows that the velocity of gas over the flat seal face (non-grooved area) is in general higher than the gas velocity over the grooved area. In addition, there are disturbances in the velocity distribution at the edges of the triangular parts of the groove. This is because of the abrupt geometrical discontinuity of the sharp edges there. These promote flow perturbations which can potentially induce fully turbulent flows. An interesting feature, observed in Figures 8a, is the influence of the groove reduces the flow

field velocity from the outer face rim to the lower rim of the contact. However, near the inner rim of the seal, the flow velocity recovers somewhat due to its remoteness from the groove. In Figure 8b, because of the existing continuum condition and no slip flow, the gas speed at the vicinity of the surface correlates well with the variation in radius. Examining the velocity contours over the groove area (Figures 8a and d), particularly over the middle trunk of groove, shows that the flow velocity increases with the depth of the groove. This is because of a closer conformance of gas flow velocity to that of the rotor surface.

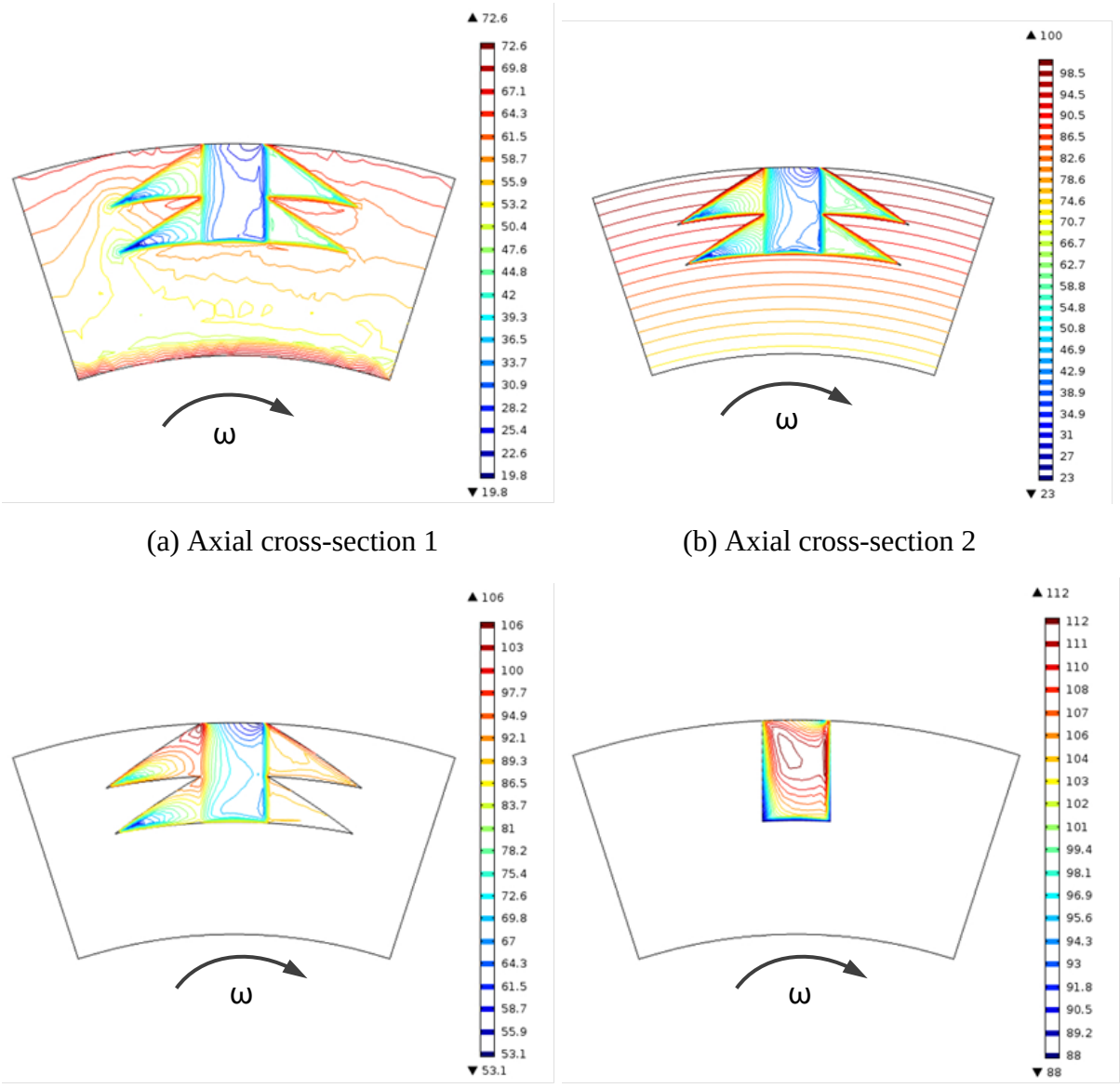

(a) Axial cross-section 1

(b) Axial cross-section 2

(c) Axial cross-section 3

(d) Axial cross-section 4

Figure 8: Contours of velocity flow field (in m/s) at different axial cross-sections

Distribution of gas temperature at different axial cross-sections is shown in Figure 9. As adiabatic boundary conditions are assumed at the inner rim of the seal and convective heat transfer its outer rim, relatively cooler conditions are observed at the gas entrance and

corresponding higher temperatures at the outlet. The higher temperatures at the outlet can also explain the rise in the velocity flow field in the outlet region, previously observed in Figure 8a. Comparing the temperature distributions in Figures 9a and 9b over the grooved region shows that the groove promotes a higher gas contact temperature. This effect is particularly clear in Figure 9b and can be attributed to the lower observed flow velocity over the grooved area (Figures 8a to d). An effect is reduced convection of heat from this region.

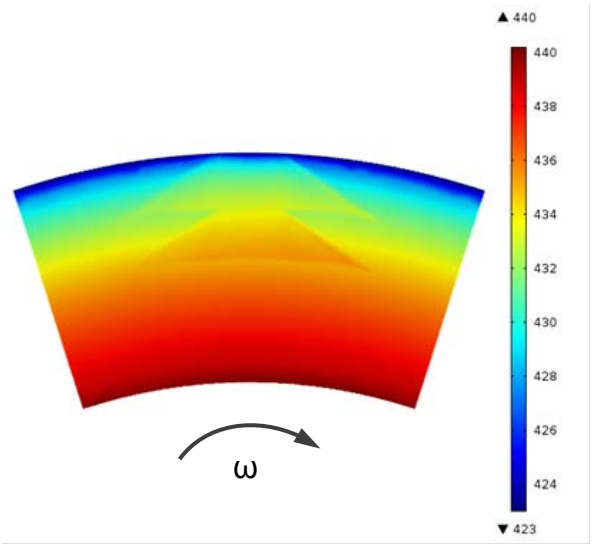

(a) Axial cross-section 1

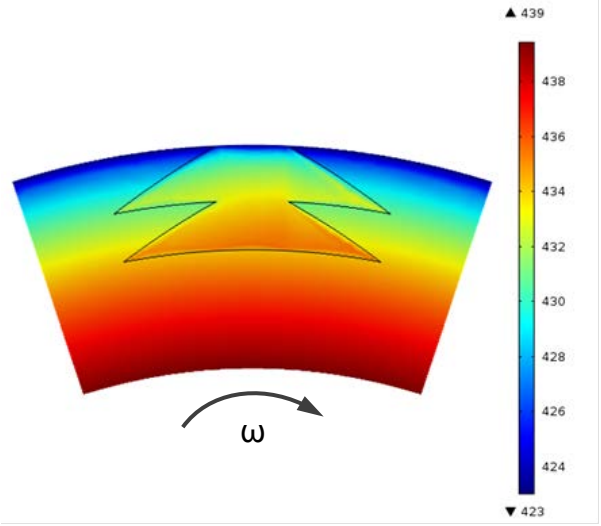

(b) Axial cross-section 2

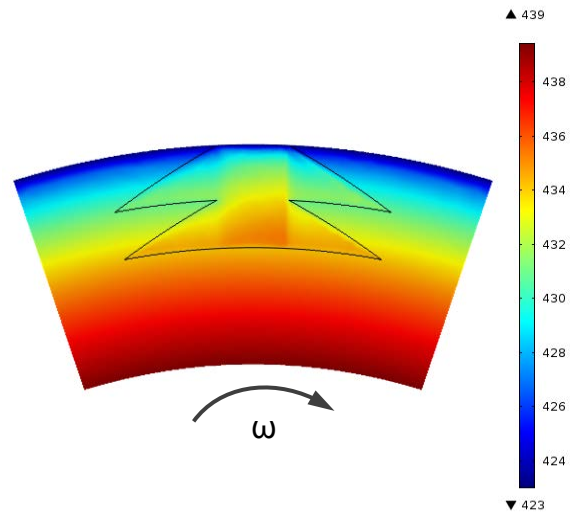

(a) Axial cross-section 1

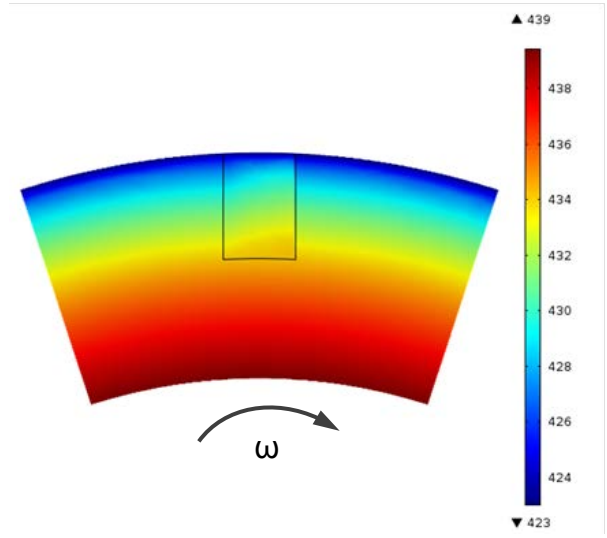

(b) Axial cross-section 2

Figure 9: Temperature distribution (in K) at different axial cross-sections

Figures 10a, b and c show the variations in gas temperature, velocity and pressure distributions in the axial cross-section 2, over the rotor surface (Figure 6a) at different radial cross-sections in Figure 6b. Figure 10a shows the gas temperature rises over the grooved area, particularly noted in groove parts closer to its outer radius (i.e. at $r = 82\text{mm}$). With an

incidence of thicker film thickness over the grooved area one would expect reduced generated heat due to reduced shear (Couette flow shear, $\tau_v = \eta V_g/h$). However, the contrary is true; because Figure 10b shows that over the grooved area the flow velocity reduces sharply, which to a large extent more than compensates for any incremental rise in the film thickness. Therefore, an alternative source for the rise noted in temperature must be sought. Examining the pressure distribution in Figure 10c sheds some light on this issue, showing a relatively sharp pressure gradient in the presence of the groove, which combined with the rise in the film thickness in this region, enhances the Poiseuille component of shear (i.e. $h(\partial p/\partial\theta)/2r$).

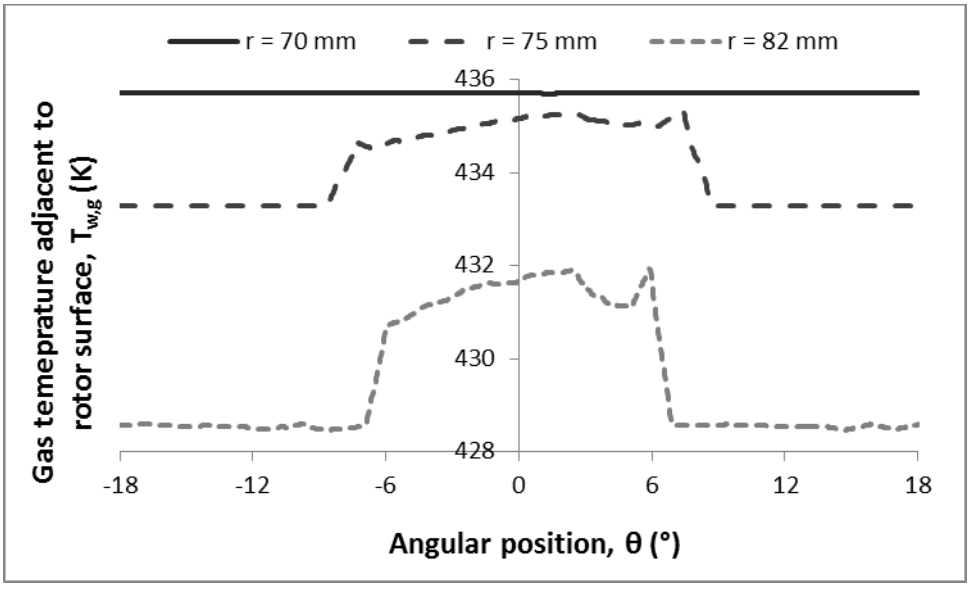

(a) Temperature

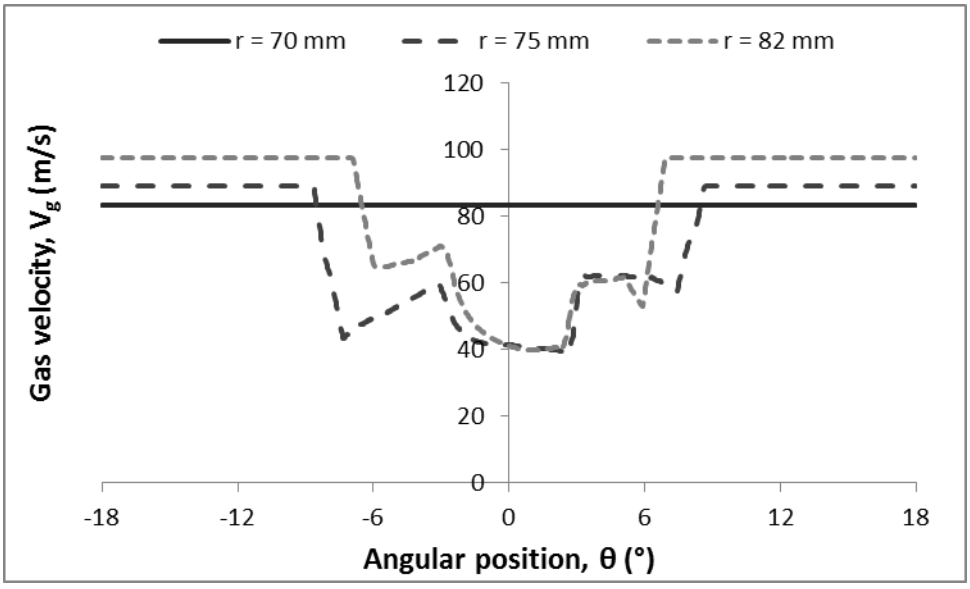

(b) Velocity

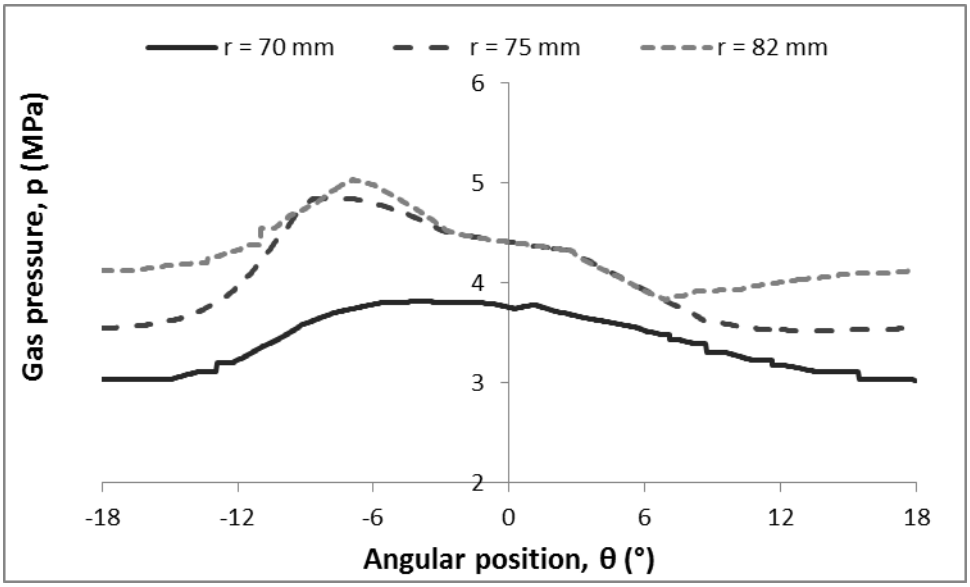

(c) Pressure

Figure 10: Gas (a) temperature, (b) velocity, and (c) pressure distributions along the circumferential direction for the radial cross-sections in Figure 6b, adjacent to the rotor surface (cross-section 2 in Figure 6a)

6.2. Effect of generated heat on gas seal performance

Predictions of a coupled thermo-hydrodynamic analysis of the bidirectional gas seal are compared with those obtained under isothermal conditions. For these analyses, the inlet pressure is $p_{in} = 4.5$ MPa and the rotational speed of the shaft is $N = 11{,}370$ RPM. In addition, two inlet gas temperatures of $T_{g,i} = 300$ K and 423 K are considered for an isothermal as well as a thermal analysis. In the isothermal analysis, the gas temperature remains constant throughout the contact domain, whilst in the thermal analysis the gas temperature alters because of the generated heat in the contact, as well as the conduction of heat to the adjacent solid barriers and partly to the environment.

The results in Figure 11 demonstrate variations of the opening force with the minimum film thickness. The results show with thinner minimum gaps, the rise in frictional losses and subsequently the viscous shear heating produces a higher opening force than that predicted under isothermal conditions. This is because the gas viscosity and hence, the load carrying capacity of the contact rises with the temperature. The rate of heat generation exceeds its dissipation through the seal faces. Conversely, with larger minimum gaps, dissipation of the heat from the contact takes place at higher rates than the rate of heat generation, resulting in a reduction in the gas viscosity of gas, which also decreases the load carrying capacity of the contact. Figure 11 clearly shows the insensitivity of the isothermal analysis to such variations in the load carrying capacity of gas seals.

It must be noted that for the given conditions the minimum gap always remains in excess of the critical minimum gap; below which asperity interactions would occur. Therefore, it can

be seen that even in the absence of boundary friction, the viscous shear of the gas generates significantly different results than those predicted under isothermal conditions.

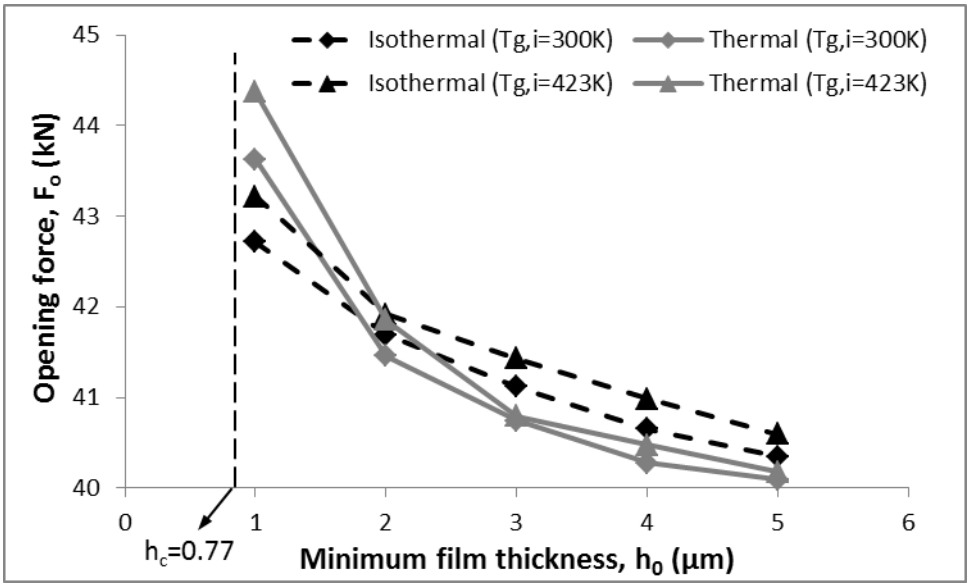

Figure 11: Comparison of predicted opening force under thermal and isothermal conditions at different minimum gaps

Figure 12, compares the predicted seal performance parameters in terms of the percentage difference in frictional power loss and volumetric leakage flow rate under thermal and isothermal conditions at different assumed minimum gaps.. The operating conditions are the same as those described for Figure 11. The percentage difference is obtained as:

$$\text{Percentage difference } (\%) = \frac{(P_l \text{ or } Q_l)_{\text{thermal}} - (P_l \text{ or } Q_l)_{\text{isothermal}}}{(P_l \text{ or } Q_l)_{\text{isothermal}}} \times 100$$

The results clearly indicate that the power loss predicted by the thermal analysis can be up to 10% higher than with isothermal analysis, particularly for lower inlet temperatures. Nevertheless, this difference seems to remain insensitive to the changes in the minimum gap.

In terms of leakage, however, the isothermal analysis seems to over-estimate the leakage from the contact, particularly with larger contact gaps, where the difference with full thermal analysis can reach up to 50%.

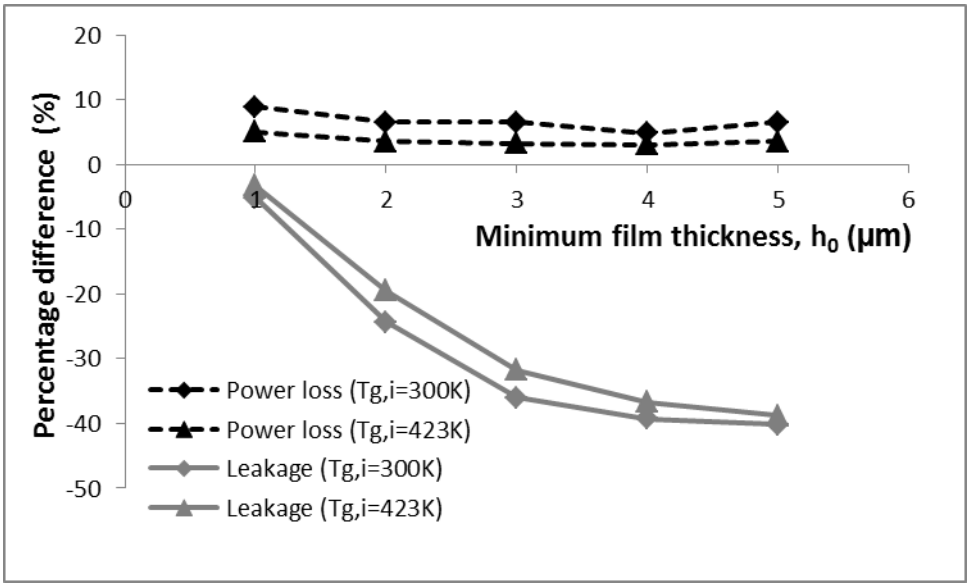

Figure 12: Comparison of the predicted seal performance parameters with thermal and isothermal analysis and with different minimum film thickness values

6.3. Evaluation of the seal performance in pure hydrodynamic and mixed regimes

For this case an inlet gas pressure of $p_{in} = 1$ MPa with a closing force of $F_c = 9.440$ kN, as well as two inlet temperatures of $T_{g,i} = 300$ K and 400 K are considered. Figure 13 shows the minimum gap obtained at various operational speeds under the stated conditions. At lower rotational speeds, the minimum film thickness crosses the critical gap line, indicating incidence of asperity interactions on the opposing surfaces.

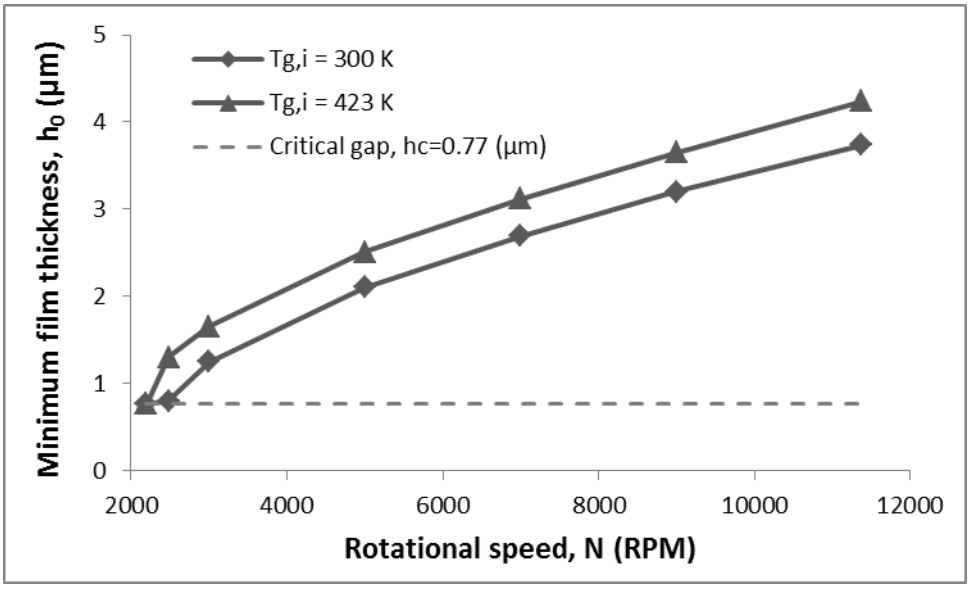

Figure 13: Calculated minimum film thickness at different operational speeds under the constant closing force of $F_c = 9.44$ kN at two different gas inlet temperatures

Figure 14 shows the power loss at inlet gas temperature of 300K. The figure shows the trend for the power loss and leakage with the rotational speed.

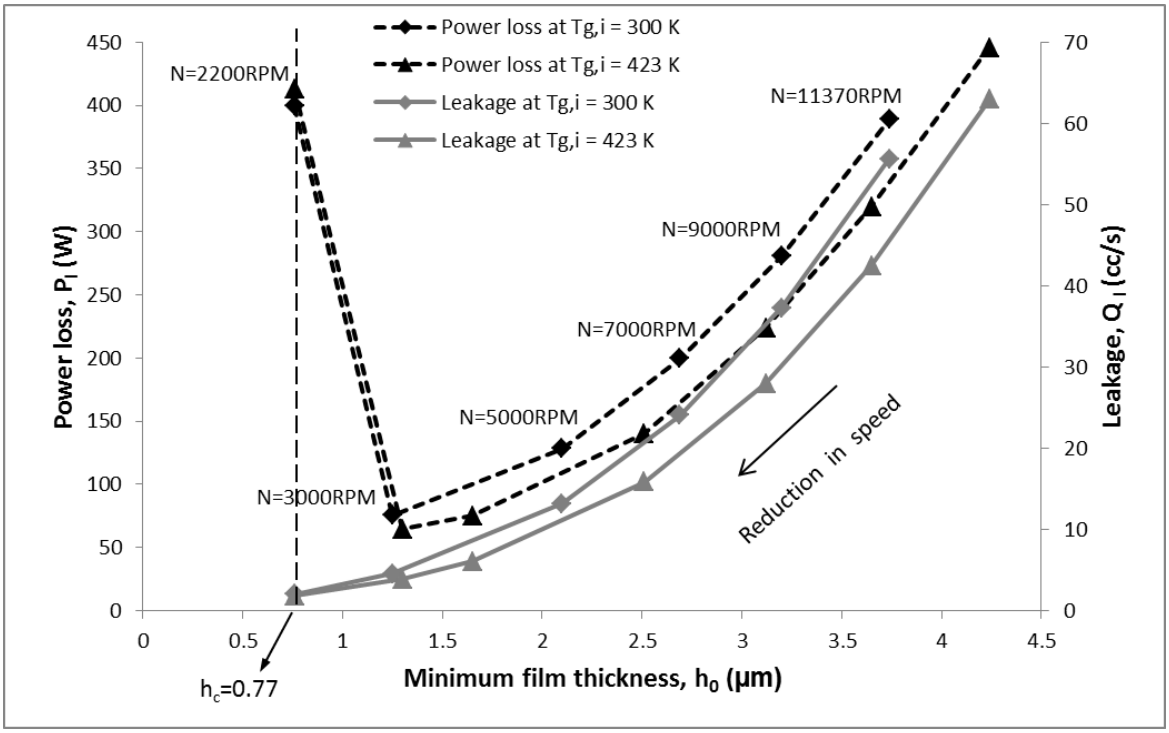

Figure 14: Power loss and leakage of seal at minimum gaps and operation speeds

As expected, both the power loss and leakage from the contact decrease as the gap diminishes until the minimum gap crosses the critical gap limit. At this point, the power loss from is abruptly increased due to increasing asperity interactions. However, the leakage from the contact attains its minimum value. A sudden rise in power loss is noted by reducing the speed of rotation from 3000RPM to 2200RPM. Therefore, at separations close to the critical gap, a relatively small change in the rotational speed can have detrimental effects on the power loss, which can possibly cause some durability issues as well due to wear. Although the minimum film thickness falls below the critical gap, due to a very large contact area of the flat part of the seal, a rapidly increasing asperity contact area can result which can lead to an excessive power loss and a corresponding rapid rise in the contact temperatures. Under these conditions global thermo-elastic distortions of the seal faces cannot be discounted, which in turn would exacerbate wear, leakage and other adverse conditions.

7. Conclusions

The current study presents a mixed thermo-hydrodynamic analysis of grooved bidirectional gas seals, incorporating realistic in-field working conditions. The model provides simultaneous solution of Navier-Stokes momentum and continuity equations with the energy equation for both the gas and the seal rings, using the COMSOL multi-physics software. In

addition, the slip flow boundary conditions are included, when required dependent on the operating conditions.

Measured topographical data using white light interferometry are used for the mixed regime of lubrication model. Additionally, AFM in lateral force mode is employed to determine the coefficient of friction at the tip of the asperities; specific to the surfaces of the seal faces.

The results from the thermal model are compared with those from an isothermal analysis, indicating that prediction of the latter lead to some unrealistic outcomes with over or under-estimation of key performance parameters.

The local variation of pressure, temperature and velocity flow field provides further in-depth knowledge of the underlying mechanisms of gas seal operation, which cannot be obtained using conventional 1D or 2D usual predictive methods.

It is shown that direct asperity contacts, in separations lower than the critical gap between the seal faces can lead to significant power loss. The sudden rise in generated heat in the contact at relatively low speeds can potentially cause durability issues.

The groove geometry produces local pressure perturbations which affect the seal performance. Further investigation of this phenomenon is necessary. It may be possible to determine an appropriate groove design, which would promotes turbulent flow; increasing the load carrying capacity and aid heat removal from the contact, thus guarding against undesired excessive thermo-elastic distortions. In addition, the contact stiffness and effect of dynamic axial vibrations should be studied for enhanced thermo-hydrodynamic performance of gas seals.

Acknowledgment

The first author wishes to express her gratitude for funding by the Chinese Scholarship Council (CSC), providing the opportunity to carry out this research at Loughborough University, UK.

The authors are grateful for the information supplied by John Crane Ltd.

References

[1] Kowalski, C.A. and Basu, P., 1995, Reverse rotation capability of spiral-groove gas face seals, Tribology Transactions, Vol. 38, pp.549-556

[2] Basu, P., 1992, Analysis of radial groove gas face seal, Tribology Transactions, Vol.35, pp. 11-20

[3] Takeuchi, T., Kataoka, T., Nagasaka, H., Kakutani, M., Ito, M. and Muraki, R., 1998, Advanced dry gas seal by the dynamic ion beam mixing technique, Proceedings of the 27th Turbomachinery symposium, pp. 39-48

[4] Wang, Y., 2004, Bi-direction rotatable face seal with spiral grooves, US Patent Publication No. 6726213 B2

[5] Goldswain, I.M. and Do Boer Hignett, M.W., 1993, Mechanical face seal with trapezoidal shaped grooves on a sealing face, US Patent 5222743 A

[6] Bonneau, D., Huitric, J. and Tournerie, B., 1993, Finite element analysis of grooved gas thrust bearings and grooved gas face seals, Journal of Tribology, Transactions of the ASME, Vol. 115, pp. 348-354

[7] Zirkelback, N., 2000, Parametric study of spiral groove gas face seals, Tribology Transactions, Vol. 43, pp. 337-343

[8] Xu, J., Peng, X., Bai, S., Meng, X., 2012, CFD simulation of microscale flow field in spiral groove dry gas seal, Proceedings of IEEE/ASME International Conference on Mechatronics and Embedded Systems and Applications (MESA), pp. 211-217, DOI: 10.1109/MESA.2012.6275564

[9] Shahin, I., Gadala, M., Alqaradawi, M. and Badr, O., 2013, Three dimensional computation study for spiral dry gas seal with constant groove depth and different tapered grooves, Procedia Engineering, Vol. 68, pp. 205-212

[10] Wang, B., Zhang, H. and, Cao, H., 2013, Flow dynamics of a spiral-groove dry-gas seal, Chinese Journal of Mechanical Engineering, Vol. 26, No. 1, pp. 78-84

[11] Su, H., Rahmani, R. and Rahnejat, H., 2016, Performance evaluation of bidirectional dry gas seals with special groove geometry, Tribology Transactions, DOI: 10.1080/10402004.2016.1146380

[12] Ruan B., Salant R. and Green I., 1997, A mixed model of liquid/gas mechanical face seal, Tribology Transactions, Vol. 40, pp. 647-657

[13] Ruan, B., 2000, Finite element analysis of the spiral groove gas face seal at the slow speed and the low pressure conditions-slip flow considerations, Tribology Transactions, Vol. 43, No. 3, pp. 411-418

[14] Brunetire, N. and Modolo, B., 2009, Heat transfer in a mechanical face seal, International Journal of Thermal Sciences, Vol. 48, pp.781-794

[15] Wang, B. and Zhang, H., 2011, Numerical analysis of a spiral-groove dry-gas seal considering micro-scale effects, Chinese Journal of Mechanical Engineering, Vol. 24, pp. 1-8

[16] Thomas, S., Brunetiere, N. and Tournerie, B., 2007, Numerical modelling of high pressure gas face seals, Journal of Tribology, Transactions of the ASME, Vol. 129, pp. 841-850

[17] Wang, H., Zhu, B., Lin, J. and Ye, C., 2013, A thermohydrodynamic analysis of dry gas seals for high-temperature gas-cooled reactor, Journal of Tribology, Transactions of the ASME, Vol. 135, pp. 021701-1 to 9

[18] Szeri, A.Z., Fluid film lubrication: theory and design, Cambridge University Press, US, 1998

[19] Munson, B.R., Young, D.F. and Okiishi, T.H., 2006, Fundamentals of fluid mechanics, 5th Ed., John Wiley & Sons, Inc. pp.272-334

[20] In-built functions available in COMSOL multi-physics software library

[21] Fukui, S. and Kaneko, R., 1988, Analysis of ultra-thin gas film lubrication based on linearized Boltzmann equation: First report – Derivation of a generalized lubrication equation including thermal creep flow, Journal of Tribology, Transactions of the ASME, Vol. 110, pp. 253-261

[22] COMSOL v.5.1 Help Documents: Microfluidics Module User's Guide, p. 204

[23] Gad-el-Hak, M., 1999, The fluid mechanics of microdevices – The Freeman Scholar Lecture, Journal of Fluids Engineering, Transactions of the ASME, Vol. 121, pp. 5-33

[24] Karniadakis, G., Beskok, A. and Aluru, N., Microflows and Nanoflows, Springer, 2005, pp. 63-67

[25] Shellef, R.A. and Johnson, R.P., 1992, A bi-directional gas face seal, Tribology Transactions, Vol. 35, No. 1, pp. 53-58

[26] Zhao, Y., Yuan, S., Hu, J. and Wei, C., 2015, Nonlinear dynamic analysis of rotary seal ring considering creep rotation, Tribology International, Vol. 82, pp. 101-109

[27] Noda, N., Hetnarski, R.B. and Tanigawa, Y., Thermal Stresses, 2nd Ed., CRC Press, New York, 2002, pp. 81-90

[28] Incropera, F.P., Dewitt, D.P., Bergman, T.L. and Lavine, S., Introduction to heat transfer, 5th Ed., John Wiley & Sons, pp. 383-433

[29] Greenwood J.A. and Tripp, J.H., 1970-71, The contact of two nominally flat rough surfaces, Proceedings of Institution of Mechanical Engineers, Vol. 185, pp. 625-633

[30] Gohar, R. and Rahnejat, H., Fundamentals of Tribology, Imperial College Press, 2008, London.

[31] Styles, G., Rahmani, R., Rahnejat, H. and Fitzsimons, B., 2014, In-cycle and life-time friction transience in piston ring–liner conjunction under mixed regime of lubrication, International Journal of Engine Research, Vol. 15, No. 7, pp. 862-876

[32] Rahmani, R., Theodossiades, S., Rahnejat, H. and & Fitzsimons, B., 2012, Transient elastohydrodynamic lubrication of rough new or worn piston compression ring conjunction with an out-of-round cylinder bore. Proceedings of the Institution of Mechanical Engineers, Part J: Journal of Engineering Tribology, Vol. 226, No. 4, pp. 284-305

[33] Wang, B., Zhang, H. and, Cao, H., 2013, Flow dynamics of a spiral-groove dry-gas seal, Chinese Journal of Mechanical Engineering, Vol. 26, No. 1, pp. 78-84